J Electroceram (2012) 28:62–69
DOI 10.1007/s10832-011-9678-z

Praseodymium-cerium oxide thin film cathodes: Study of oxygen reduction reaction kinetics

Di Chen · Sean R. Bishop · Harry L. Tuller

Received: 13 October 2011 / Accepted: 25 December 2011 / Published online: 17 January 2012

Abstract Praseodymium-Cerium Oxide ($Pr_xCe_{1-x}O_{2-\delta}$; PCO), a potential three way catalyst oxygen storage material and solid oxide fuel cell (SOFC) cathode, exhibits surprisingly high levels of oxygen nonstoichiometry, even under oxidizing (e.g. air) conditions, resulting in mixed ionic electronic conductivity (MIEC). In this study we examine the redox kinetics of dense PCO thin films using impedance spectroscopy, for x=0.01, 0.10 and 0.20, over the temperature range of 550 to 670°C, and the oxygen partial pressure range of 10^{-4} to 1 atm O_2. The electrode impedance was observed to be independent of electrode thickness and inversely proportional to electrode area, pointing to surface exchange rather than bulk diffusion limited kinetics. The large electrode capacitance (10^{-2}F) was found to be consistent with an expected large electrochemically induced change in stoichiometry for x=0.1 and x=0.2 PCO. The PCO films showed surprisingly rapid oxygen exchange kinetics, comparable to other high performance SOFC cathode materials, from which values for the surface exchange coefficient, k^q, were calculated. This study confirms the suitability of PCO as a model MIEC cathode material compatible with both zirconia and ceria based solid oxide electrolytes.

D. Chen (✉) · S. R. Bishop · H. L. Tuller
Department of Materials Science and Engineering,
Massachusetts Institute of Technology,
Cambridge, MA 02139, USA
e-mail: dichen@mit.edu

S. R. Bishop
International Institute for Carbon Neutral Energy Research
(I2CNER), Kyushu University,
Nishi-ku,
Fukuoka 819-0395, Japan

Keywords Ceria · Three-way catalyst · Oxygen storage · Oxygen separation · Permeation membrane mixed ionic electronic conduction · Solid oxide fuel cell

1 Introduction

Cerium dioxide (ceria, CeO_2) and ceria related materials have been used extensively in automotive exhaust three way catalysts (TWCs) [1, 2] and are prime candidates for the oxygen electrolyte and electrodes in solid oxide fuel cells (SOFCs) [3]. The latter applications are based on the high oxygen ion conductivity of ceria upon doping with acceptor ions such as trivalent Gd [4] and Sm [5, 6] as well as its mixed ionic electronic conduction (MIEC) in reducing atmospheres [7]. The TWC application derives from the ability of ceria to store and release oxygen, related to the existence of the Ce^{4+}/Ce^{3+} redox couple in oxidizing (e.g. NO_x) and reducing (e.g. C_xH_y, CO) atmospheres, respectively. The oxygen storage capacity of ceria in TWCs is normally further enhanced by the addition of Zr [8]. In addition to fixed valence additives (e.g. Gd^{3+} and Zr^{4+}), it is also possible to substitute elements that exhibit multiple valences with changing temperature and oxygen partial pressure (pO_2). One such element, Pr, is particularly interesting given its similar ionic radius to that of Ce, leading to a wide solid solubility with ceria, and its ready reduction from Pr^{4+} to Pr^{3+} even under oxidizing conditions [7, 9].

The authors and others have reported on the defect and transport properties of the $Pr_xCe_{1-x}O_{2-\delta}$ solid solution system (PCO) and found it to have an ionic conductivity comparable to that of Gd doped ceria (GDC) but with a significant electronic contribution at high pO_2 due to electron hopping between adjacent Pr ions [9–12]. Furthermore, high levels of oxygen nonstoichiometry ($\delta \approx x/2$) are already achieved at

$pO_2 > 10^{-8}$ atm, i.e. at pO_2's much above that needed to reach similar levels of δ in un-doped ceria. Given its MIEC character, together with oxygen deficiency under relatively oxidizing (e.g. air) conditions, $Pr_xCe_{1-x}O_{2-\delta}$ serves well as a model system to examine SOFC cathode [13] and TWC oxygen storage material [14] properties.

The key figures of merit for performance of SOFC cathodes and TWC materials include the rate at which oxygen exchanges between gas and solid phases, the magnitude of the oxygen diffusivity through the lattice, and the change in stoichiometry (δ). The main objective of this study is to examine the first figure of merit: oxygen incorporation reaction rate as a function of Pr concentration, temperature, and pO_2. Well defined and reproducible, dense PCO thin films with different Pr levels are prepared by pulsed layer deposition (PLD) and deposited onto yttria-stabilized zirconia (YSZ) single crystal substrates. In this way, the geometry of the films could be well defined, thereby allowing for a quantitative analysis of their electrochemical properties by normalization of the experimental data with respect to geometry, such as triple phase boundary length (TPBL), surface area, and film thickness [15–17]. Electrochemical impedance spectroscopy (EIS) was used to aid in the deconvolution of bulk and interfacial processes, resulting in the isolation of the surface exchange contribution to the electrode impedance for the present work. The results are examined in relation to the defect structure and bulk transport properties of PCO.

2 Experimental

$Pr_xCe_{1-x}O_{2-\delta}$ films with x=0.01, 0.1, 0.2 (denoted throughout the text as PCO100x; i.e. PCO10 is for x=0.1) were prepared by PLD from oxide targets. The films were deposited onto (001) oriented single crystal YSZ (8 mol% Y_2O_3 stabilized) substrates ($10\times10\times0.5$ mm^3; MTI Corporation, Richmond, CA). 2.5 cm diameter oxide targets were fabricated from PCO powders prepared through a Pechini-based gel process described briefly below [18]. The following starting materials were utilized: cerium (III) nitrate hexahydrate, 99.99% (Sigma Aldrich), praseodymium (III) nitrate hydrate, 99.9%, ethylene glycol (Alfa Aesar) and anhydrous citric acid (Fisher Scientific). Citric acid and ethylene glycol were mixed with aqueous solutions of $Ce(NO_3)_3$ and $Pr(NO_3)_3$ at 80°C until polyesterification resulted in the formation of a gel. After drying in an oven at 110°C, the as-obtained powder was fired at 450°C for 4 hours and then at 700°C for 3 hours in flowing air. The PCO powders were examined by X-ray diffraction (Rigaku H3R Cu-source Powder Diffractometer) and were found to have a single phase fluorite structure. Dense PLD targets were then prepared by isostatic pressing PCO powder followed by sintering at >1400°C.

The PLD system (Neocera Inc., Beltsville, ML) was operated with a KrF excimer laser (Coherent COMPex Pro 205), emitting at 248 nm, at energy of 400 mJ/pulse and with a repetition rate of 8 Hz. The substrates were heated to 725°C during deposition, while the oxygen pressure was maintained at 10 mTorr after pumping the background pressure to less than 9×10^{-6} Torr. Following deposition and prior to cooling, the oxygen pressure in the chamber was increased to approximately 6–7 Torr to facilitate more complete oxidation of the films. A stainless steel mask with holes to produce 1 and 2 mm diameter and 4 mm×4 mm and 9 mm×9 mm square films was used to fabricate PLD films with different surface areas.

Figure 1 is a photograph of an approximately 9 mm×9 mm PCO film prepared by PLD. Its reddish color is a consequence of a photon induced transition of electrons from the ceria valence band to Pr^{4+} levels lying within the ceria band gap [19].

Film structure characterization was performed using x-ray diffraction (XRD; X'Pert PRO MPD, PANalytical). Approximate grain size and surface roughness were measured by atomic force microscopy (Digital Instruments Nanoscope IIIa), while film thickness, ranging between 100 and 500 nm, was determined by taking the height difference with a surface profilometer (KLA-Tencor P-16+ stylus profiler) between masked and unmasked areas.

Two different sample geometries were prepared for EIS measurements: a symmetrical structure with identically sized (9×9 mm^2) PCO electrodes on both sides of the YSZ electrolyte, and an asymmetrical structure of 1–10 mm diameter PCO working electrodes with a porous Ag counter electrode (SPI Silver Paste Plus, SPI Supplies, Chester, PA, USA) on the opposite side of the YSZ substrate/electrolyte. In both configurations, Au paste (Fuel cell materials, Lewis Center, Ohio), serving as a current collector, was applied to the top surface of the PCO electrode.

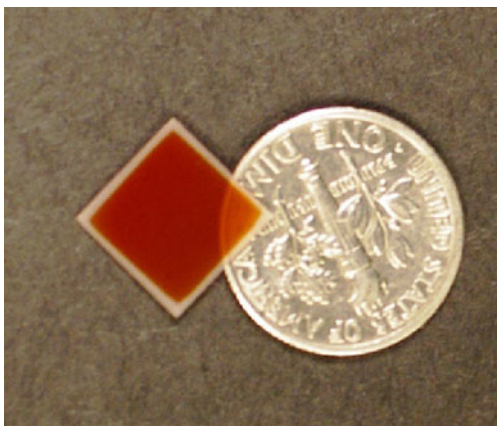

Fig. 1 Photograph of a PCO10 film deposited onto a YSZ substrate by PLD

The EIS measurements were performed at temperatures between 550 and 670°C and oxygen partial pressures between 2×10^{-4} and 1 atm controlled by mixing N2 and O2 with the aid of mass flow controllers and monitored by an in-situ YSZ Nernst type oxygen sensor. EIS measurements, covering the frequency range from 1 MHz to 0.032 Hz, with AC amplitude of 20 mV, were performed using an impedance analyzer (Solartron 1260) and fit with equivalent circuits using Zview and Zplot software (Scribner Associates).

3 Results and discussion

3.1 Film characterization

Figure 2 shows the XRD pattern obtained from 2θ-ω coupled scans of the YSZ single crystal with (Fig. 2(a)) and without the 10PCO film (Fig. 2(b)). Only the {001} peaks are observed for the film, which confirm that the PLD films exhibited the fluorite structure with highly (100) oriented texture.

Surface analysis by AFM showed a dense and smooth film indicating a grain size of approximately 50 nm and surface roughness of approximately 0.5 nm.

3.2 Impedance spectra and model

Figure 3 shows typical impedance results obtained for the asymmetric cell. The spectrum exhibits two adjacent semicircles offset from the origin. The one at higher frequencies is smaller and more highly distorted. The second, at lower frequency, is larger and is a near-ideal semicircle.

One can assign this response to a resistor in series with two *R*-*Q* circuits (*R*-*Q*: a resistor in parallel with a constant phase element [CPE]) as shown by the inset in Fig. 3. The three resistors are defined as R_{off}, R_H and R_L and their origins are defined later. CPEs are used given that electrode impedances are typically characterized by a distribution of time constants resulting from morphological variations within the electrode and at the electrode/electrolyte interfaces resulting in "depressed" arcs not well represented by an ideal capacitor [20]. The impedance of a constant phase element is given by

$$Z = \frac{1}{Q(i\omega)^n} \tag{1}$$

from which the capacitance is derived using the following equation [21]

$$C = Q\omega_{\max}^{n-1} = \left(R^{1-n}Q\right)^{\frac{1}{n}} \tag{2}$$

The fit, applying the equivalent circuit (shown in the inset of Fig. 3) to the data, is observed to be quite good.

3.3 Origin of R_{off}

Several features of the offset resistance (R_{off}) are consistent with the YSZ single-crystal substrate. This includes the

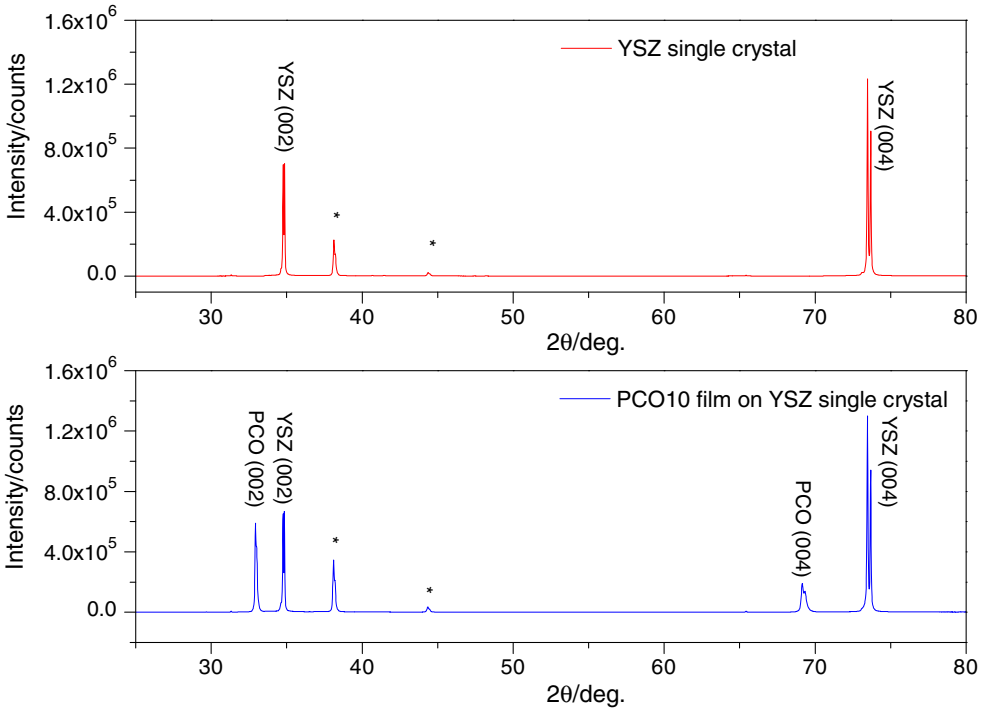

Fig. 2 XRD analysis of the as-deposited PCO10 film on YSZ (001) substrate (**a**) XRD 2θ-ω coupled scan on YSZ single crystal substrate; (**b**) XRD 2θ-ω coupled scan on PCO10 film deposited on YSZ single crystal substrate. The asterisks denote peaks from secondary radiation (i.e. non-Cu-k_α radiation)

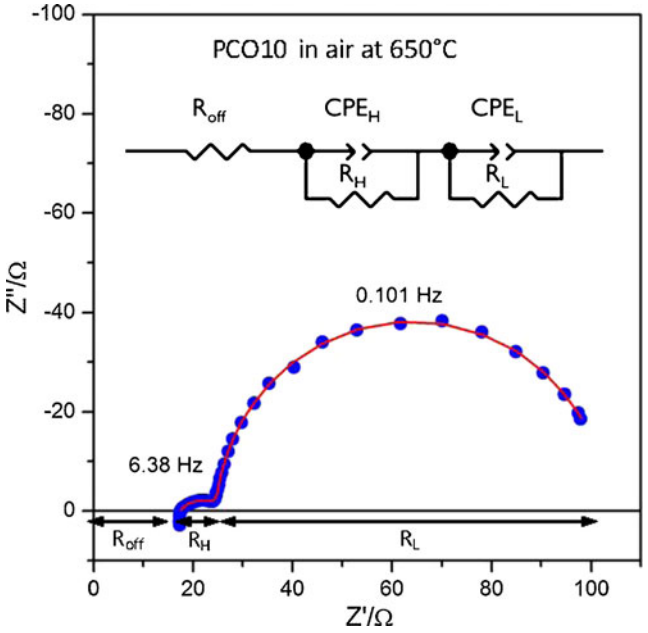

Fig. 3 Typical impedance spectra of an asymmetric cell of PCO10/YSZ/Ag at 650°C in air, where variables are defined in the text. Film thickness is 249 nm and the denoted frequencies correspond to the top, or peak, point in their respective semi-circles. Inset shows the equivalent circuit fit to the data using the Zview program.

activation energy, its pO_2 independence, and its magnitude of conductivity.

In Fig. 4(a), R_{off}, extracted from the impedance spectra obtained for the asymmetric cell, and normalized to the geometry of the cell, is plotted as log σT vs T^{-1} to facilitate calculation of an activation energy (E_A) consistent with the following equation for ionic conductivity.

$$\sigma = \frac{\sigma_\circ}{T} \exp\left(-\frac{E_A}{kT}\right) \tag{3}$$

The data obtained in this study are characterized by E_A=1.14±0.03 eV, typical of values obtained for ionic conduction in YSZ [23]. In Fig. 4(b), the offset resistance is recalculated as above and plotted as logσ vs log pO2, and within the experimental error, one finds that this resistance is independent of pO_2, consistent with acceptor (Y) doped zirconia. R_{off} derived from the impedance spectra of cells using PCO1 and PCO20 exhibit a similar temperature and pO2 dependence. One can thus confidently conclude that R_{off} simply reflects the series YSZ ohmic contribution to the overall cell impedance.

3.4 Origin of R_H and C_H

Figure 5 shows impedance results obtained for both the symmetric and asymmetric structures for PCO10 samples. Going from the asymmetric to the symmetric cell, the high

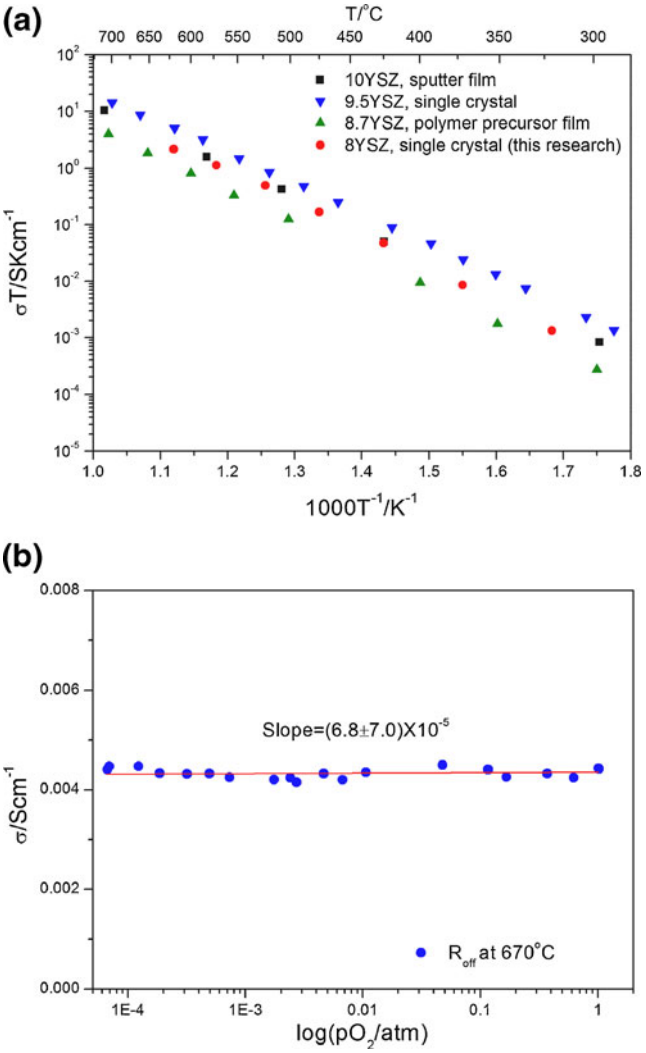

Fig. 4 (**a**) Temperature dependence of σT extracted from R_{off} using the substrate size in the conductivity calculation for a PCO10 sample in air and, compared with: 10 mol% YSZ film [22], 9.5 mol% YSZ single crystal [23], and 8.7 mol% YSZ film [24] (**b**) Oxygen partial pressure dependence of σ calculated from R_{off}

frequency semicircle disappears while the diameter of the low frequency semicircle doubles in magnitude. Given that the only features in the impedance spectrum of the symmetric structure is the semicircle with diameter of 155 Ω and the previously defined R_{off}, the semicircle can confidently be assigned to the PCO electrodes, with each electrode contributing half this value (~77 Ω). On the other hand, the asymmetric structure exhibits both a small distorted high frequency semicircle with a 9.5 Ω diameter and a nearly ideal low frequency semicircle with a 79.9 Ω diameter. Comparing the two structures, it becomes obvious that in the asymmetric structure, the larger low frequency semicircle (roughly half that in the symmetric structure) should be assigned to the PCO electrode, while the smaller high frequency semicircle (characterized by R_H and C_H) should be attributed to the porous Ag electrode.

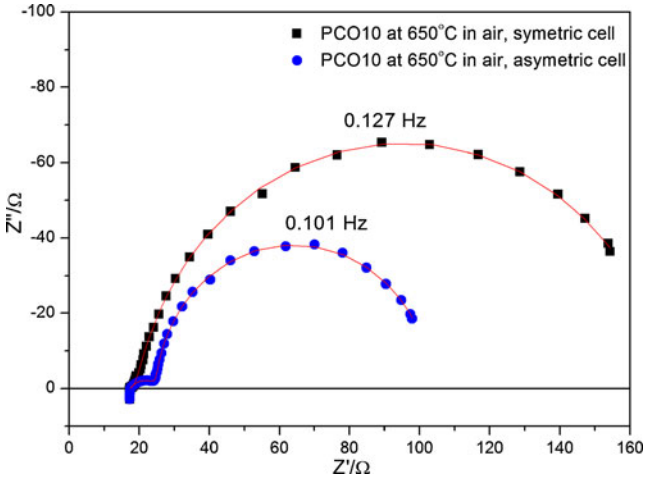

Fig. 5 Complex Impedance plot of symmetric and asymmetric cell of PCO10 at 650°C in air with peak frequencies indicated

3.5 Origin of R_L and C_L

Given the ability to confirm that the low frequency semicircle comes from the PCO electrode, the R and C values derived from this part of the impedance spectra are therefore designated as R_{PCO} and C_{PCO}. In the following, the focus shifts to identifying the electrode processes controlling R_{PCO} and C_{PCO}.

In an MIEC electrode, three key rate limiting processes need to be considered for oxygen transport from the gas phase into the dense electrode and ultimately into the electrolyte [19]. These are (i) oxygen surface exchange at the electrode-gas interface, (ii) mass transport through the electrode, and (iii) transfer of oxygen ions across the PCO/YSZ interface. In electrodes like $La_{1-x}Sr_xMnO_3$ which are not significant MIECs (i.e. they display predominant electronic with minimal ionic conduction), oxygen reduction and insertion at the triple phase boundary (TPB) between electrode, electrolyte, and gas phase dominates (Fig. 6). The oxygen insertion process thus will have different dependencies on electrode geometry depending on whether, for example, the exchange reaction is limited to the TPB or can occur anywhere along the 2 phase boundary (electrode surface). In addition, reaction products can form at the electrode/electrolyte interface, blocking ion transport.

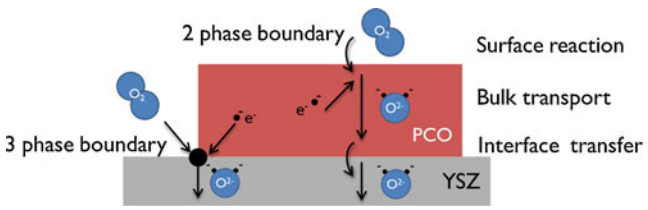

Fig. 6 Typical dominant reaction paths for oxygen reduction on MIEC (2-phase boundary) and non MIEC (3 phase boundary) electrodes

As the use of dense thin-film electrodes enables one to easily control geometry, one can deduce the dominant reaction site(s) by obtaining a quantitative relationship between electrode impedance and geometry. These relationships are summarized in Table 1.

Log *R*PCO for PCO10 is plotted vs. log (electrode area, S) in Fig. 7 and shows a power law dependence of −1. One can thus conclude that the oxygen reduction reaction occurs over the full electrode surface area of PCO, rather than being limited to the TPB (see Table 1), as also reported for thin-film $SrTi_xFe_{1-x}O_{3-\delta}$ (STF) [25], $La_{1-x}Sr_xCoO_{3-\delta}$ (LSC), and $La_{1-x}Sr_xCo_{1-y}Fe_yO_{3-\delta}$ (LSCF) [26] MIEC electrodes. In Fig. 8, log *R*PCO vs T^{-1} is plotted with film thicknesses varying by as much as a factor of 3. R_{PCO} is observed, within experimental error, to be independent of film thickness, confirming that oxygen diffusion through the film (Bulk transport in Table 1) is not controlling the electrode response. R_{PCO} for PCO1 and PCO20 films showed a similar geometrical dependence. Lastly, a blocking tertiary phase is not expected (nor observed via XRD) at the electrode/electrolyte interface since both YSZ and PCO exhibit the fluorite structure and indeed other studies intentionally use doped ceria as a protective buffer layer to avoid a reaction product to form between, for example, LSC and YSZ [14, 27]. We are thus confident in concluding that R_{PCO} is limited by surface exchange kinetics for all three PCO compositions studied here.

Next, turning to C_L (=C_{PCO}), it too has different possible origins. These are (i) Bulk capacitance, (ii) capacitance at the electrode-electrolyte interface, and (iii) defect concentration dependent chemical capacitance. As in the resistance study, one can also deduce the type of capacitance by controlling the sample geometry (Table 2).

Log *C*PCO for PCO10 is plotted vs. logS in Fig. 7 and shows a power law dependence of 1. In Fig. 9, log *CPCO* is plotted vs. log h, and shows a power law dependence of 1. Both of these results point to the capacitance as being "chemical capacitance". The fact that the fitted line in Fig. 9 passes through the origin, further confirms the absence of interfacial capacitance contributions (interface capacitance typically results in an offset on the y axis of Fig. 9 [28]). PCO1 and PCO20 show a similar geometrical dependence of capacitance as PCO10. Additionally, the *CPCO* values are exceptionally high, e.g. 25.0 mF/cm^2 for a 333.4 nm thick PCO10 film at 670°C (typical n value between 0.979 and 0.997, see

Table 1 Possible origin of R_{PCO} and its geometric dependences

	Surface Area (S)	Film Thickness (h)
Surface exchange	$R \propto S^{-1}$	$R \propto h^0$
Bulk transport	$R \propto S^{-1}$	$R \propto h^1$
TPB	$R \propto S^{-1/2}$	$R \propto h^0$

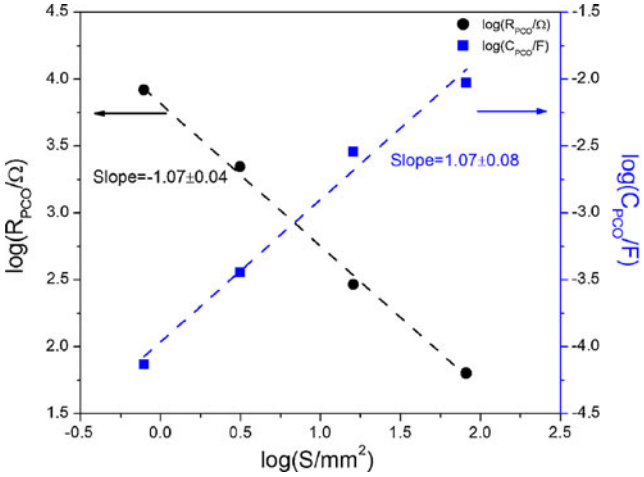

Fig. 7 Double-logarithmic plots of R_{PCO} and C_{PCO} for the PCO10 electrode vs surface area (S), measured at 670°C in air using the asymmetric cell configuration

Eq. 2), in agreement with the magnitude of chemical capacitance reported in other thin film MIEC systems [25, 29]. The authors will be presenting a more detailed analysis of PCO thin film chemical capacitance in a forthcoming publication.

3.6 Surface exchange

3.6.1 Values for the area specific resistance and surface exchange coefficient

Since the surface exchange reaction has been identified as being the rate limiting process for oxygen exchange, the corresponding surface exchange rate coefficient can now be extracted from the measured electrode resistance. Previously, the electrically derived surface oxygen exchange coefficient

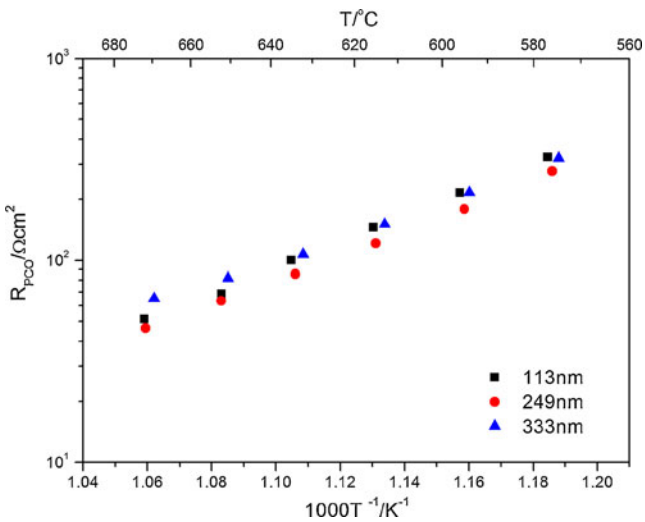

Fig. 8 Temperature dependence of R_{PCO} for PCO10 electrodes with three different film thicknesses, as indicated. Measured in air using the asymmetric cell configuration

Table 2 Possible origin of C_{PCO} and its geometry dependence

	Surface Area S	Film Thickness h
Bulk capacitance	$C \propto \propto S^1$	$C \propto h^{-1}$
Interfacial capacitance	$C \propto S^1$	$C \propto h^0$
Chemical capacitance	$C \propto S^1$	$C \propto h^1$

(k^q) has been defined as inversely proportional to the resistance as [30]

$$k^q = \frac{kT}{4e^2 R_S c_O} \tag{4}$$

Where k is the Boltzmann constant, e is the electron charge, T is the temperature, Rs is the area specific resistance (equal to R_{CPO}), and c_O is the total concentration of lattice oxygen (~5.04×10^{22} cm^{-3}).

Calculated k^q values are listed in Table 3. Further confirmation of surface exchange control can be obtained by examining the so-called characteristic thickness L_C, the ratio of the oxygen self-diffusion coefficient and the corresponding surface exchange coefficient, $LC = D^*/k^q$ [25, 31], above which mass transport through the electrode thickness becomes dominant relative to the surface exchange reaction. Values for the oxygen diffusion coefficient are derived from an analysis of electrical conductivity measurements performed on PCO [10]. The characteristic thickness of PCO10 and PCO20 at 670°C is approximately 3.58×10^3 and 2.20×10^3 μm, respectively, much thicker than the PCO film thicknesses used in this work. Furthermore because LC becomes thicker with decreasing temperature, given the larger activation energy of k^q than D^*, it is clear that the surface exchange reaction remains dominant in the temperature range of this work, 550–670°C.

R_S and k^q obtained for dense thin films of other MIEC electrodes prepared by PLD are compared in Fig. 10 with

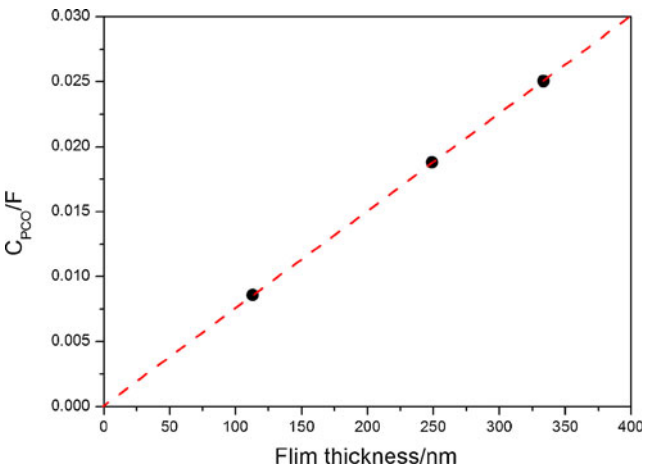

Fig. 9 Thickness dependence of C_{PCO} of a PCO10 electrode measured at 670°C in air using the asymmetric cell configuration

Table 3 Surface exchange coefficient, oxygen self-diffusion coefficient and characteristic thickness of PCO with different Pr concentrations

	k^q (cm/s)	D^* (cm^2/s)	L_c (μm)
PCO1	1.38×10^{-8}	2.31×10^{-9}	1.68×10^{3}
PCO10	3.73×10^{-8}	1.34×10^{-8}	3.58×10^{3}
PCO20	4.59×10^{-8}	1.01×10^{-8}	2.20×10^{3}

PCO, helping to ensure that morphology differences between typical bulk MIEC electrodes and the dense thin film PCO electrodes used in this study played no role in influencing comparison of performance. The R_S and k^q values for PCO are comparable with those of LSC, LSCF and STF pointing to the suitability of PCO as a realistic model MIEC cathode material. Interestingly, as shown in Table 4, PCO displays high k^q values despite having a considerably lower electronic conductivity than the previously listed cathode materials (a high value is often suggested as a necessity for high k^q [33]). The origin of this unexpected phenomenon is under further investigation.

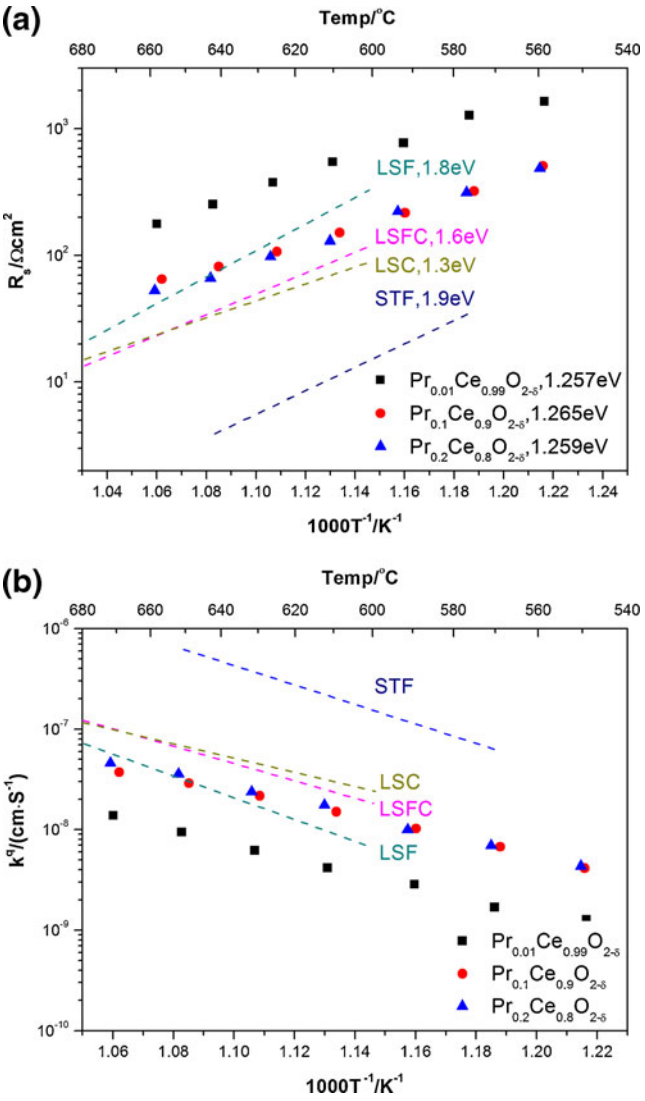

Fig. 10 Temperature dependence of R_S=R_{PCO} (**a**) and k^q (**b**) of PCO compared with other dense thin-film MIEC electrodes fabricated by PLD: $La_{0.6}Sr_{0.4}FeO_{3-\delta}$ [26], $La_{0.6}Sr_{0.4}Fe_{0.8}Co_{0.2}O_{3-\delta}$ [26], $La_{0.6}Sr_{0.4}CoO_{3-\delta}$ [26] and $SrTi_{0.5}Fe_{0.5}O_{3-\delta}$ [25]

Table 4 Surface exchange coefficient, electronic and ionic conductivity, and electronic transfer numbers at 800°C in air (k^q for PCO are extrapolated to high temperature, enabling comparison with STF and LSCF)

	k^q(cm/s)	σ_{el}(S/cm)	σ_{ion}(S/cm)	t_e
PCO1	1.02×10^{-7}	2.91×10^{-5}	3.21×10^{-3}	0.009
PCO10	3.90×10^{-7}	1.73×10^{-2}	2.64×10^{-2}	0.396
PCO20	4.75×10^{-7}	3.48×10^{-2}	1.89×10^{-2}	0.648
$SrTi_{0.5}Fe_{0.5}O_{3-\delta}$[15]	1.7×10^{-5}	1.8	3.6×10^{-2}	0.9804
$La_{0.6}Sr_{0.4}Co_{0.2}Fe_{0.8}O_3$[32]	5.6×10^{-6}	3.02×10^{2}	8×10^{-3}	0.9997

3.6.2 *Temperature and pO2 dependence of R_{PCO}*

The activation energies (E_A) derived from, the Arrhenius dependence of R on reciprocal temperature

$$R = R_\circ \exp(-E_A/kT) \quad (5)$$

for PCO1, PCO10, and PCO20 in air for temperatures from 550°C to 670°C are compared with other MIEC materials in Fig. 10 and one finds that they are closest to that of LSC, i.e. ~1.3 eV.

The pO2 dependence of the electrode resistance is shown in Fig. 11 in the form of a log-log plot. The slope is close to

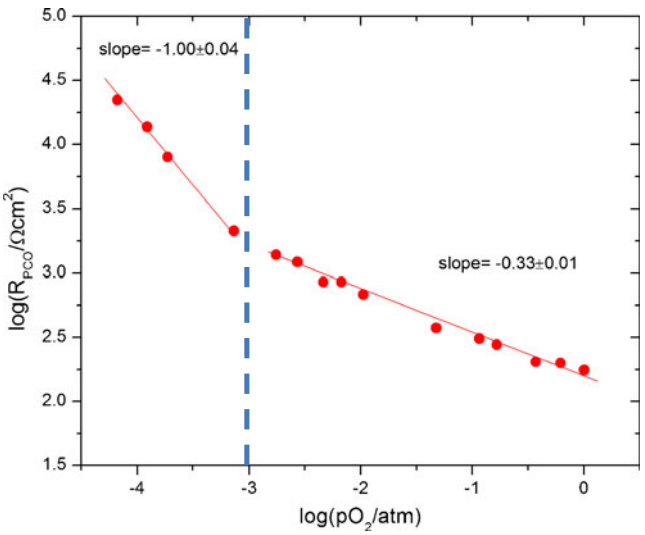

Fig. 11 pO_2 dependence of R_{PCO} of PCO10 at 670°C. The pO_2 at which an apparent transition in rate limiting mechanism occurs is indicated by the vertical *dashed line*

−1/3 at high pO_2 and close to −1 at low pO_2. This implies a mechanism change between the two regions. A similar shift in pO_2 dependence of the electrode resistance in the $SrTi_{1-x}Fe_xO_{3-\delta}$ was ascribed to a shift from charge transfer control at high pO_2 to the availability of adsorbed oxygen species at low pO2 [32]. The source of this observation in the PCO system is under further investigation.

4 Conclusions

PCO cathodes, prepared as dense films with well-defined area and thickness, were demonstrated to exhibit typical MIEC behavior with the electrode reaction occurring over the full electrode surface area, rather than being limited to the TPB. The electrode impedance was observed to be independent of electrode thickness and inversely proportional to electrode area, pointing to surface exchange rather than bulk diffusion limited kinetics. The large measured chemical capacitance (10^{-2} F) was found to be consistent with an expected large electrochemically induced change in stoichiometry of the PCO10 and PCO20 electrodes, further confirming the electrode controlled surface exchange reaction.

The PCO films showed surprisingly low oxygen exchange resistances between 550 and 670°C. Values for the surface exchange coefficient, k^q, were calculated and found to be comparable in magnitude to those exhibited by other high performance MIECs such as LSC and LSCF, thereby confirming the suitability of PCO as a model high performance MIEC cathode material, in spite of the fact that the electronic conductivity of PCO is several orders of magnitude lower than that of typical perovskite MIEC electrodes. Furthermore, PCO, in contrast to many perovskite based cathodes, is expected to be chemically compatible with both zirconia and ceria based solid oxide electrolytes.

Acknowledgments This work was supported by the National Science Foundation Materials World Network in collaboration with Prof. Moos, Universität Bayreuth, Germany under grant No. DMR-0908627. The authors thank Dr. WooChul Jung, MIT (now at Caltech), for providing constructive discussions, Mr. Jae Jin Kim for preparation of the PLD targets and the Center of Materials Science and Engineering (NSF-MRSEC) at MIT for use of its facilities. SRB recognizes partial support from I^2CNER.

References

1. M. Boaro, A. Trovarelli, J.H. Hwang, T.O. Mason, Solid State Ionics **147**, 85 (2002)
2. S. Bernal, G. Blanco, J.J. Calvino, J.M. Gatica, J.A.P. Omil, J.M. Pintado, Top. Catal. **28**, 31 (2004)
3. S. Haile, Mater. Today **6**, 24 (2003)
4. B.C.H. Steele, Solid State Ionics **129**, 95 (2000)
5. K. Eguchi, T. Setoguchi, T. Inoue, H. Arai, Solid State Ionics **52**, 165 (1992)
6. S. Gupta, S.V.N.T. Kuchibhatla, M.H. Engelhard, V. Shutthanandan, P. Nachimuthu, W. Jiang, L.V. Saraf, S. Thevuthasan, S. Prasad, Sensor Actuator B Chem **139**, 380 (2009)
7. K.L. Duncan, Y. Wang, S.R. Bishop, F. Ebrahimi, E.D. Wachsman, J. Am. Ceram. Soc. **89**, 3162 (2006)
8. M. Boaro, C.D. Leitenburg, G. Dolcetti, A. Trovarelli, J. Catal. **193**, 338 (2000)
9. S.R. Bishop, T.S. Stefanik, H.L. Tuller, Phys. Chem. Chem. Phys: PCCP **13**, 10165 (2011)
10. T.S. Stefanik, *Electrical Properties and Defect Structure of Praseodymium-Cerium Oxide Solid Solutions, in Department of Materials Science and Engineering* (Massachusetts Institute of Technology, Cambridge, 2004)
11. S.R. Bishop, D. Chen, Y. Kuru, J.J. Kim, T.S. Stefanik, H.L. Tuller, ECS Trans. **33**, 51 (2011)
12. S.R. Bishop, J.J. Kim, N. Thompson, D. Chen, Y. Kuru, T.S. Stefanik, H.L. Tuller, ECS Trans. **35**, 1137 (2011)
13. R. Chiba, T. Komatsu, H. Orui, H. Taguchi, K. Nozawa, H. Arai, ECS Trans. **26**, 333 (2010)
14. M.Y. Sinev, G.W. Graham, L.P. Haack, M. Shelef, J. Mater. Res. **11**, 1960 (1996)
15. W. Jung, H.L. Tuller, Solid State Ionics **180**, 843 (2009)
16. J. Fleig, F.S. Baumann, V. Brichzin, H.R. Kim, J. Jamnik, G. Cristiani, H.U. Habermeier, J. Maier, Fuel Cells **6**, 284 (2006)
17. G.J. la O', B. Yildiz, S. McEuen, Y. Shao-Horn, J. Electrochem. Soc. **154**, B427 (2007)
18. K. Masato, Y. Masahiro, Bull. Chem. Soc. Jpn **72**, 1427 (1999)
19. H.L. Tuller, S.R. Bishop, Annu. Rev. Mater. Res. **41**, 369 (2011)
20. S.B. Adler, Chem. Rev. **104**, 4791 (2004)
21. J. Fleig, Solid State Ionics **150**, 181 (2002)
22. E.S. Thiele, L.S. Wang, T.O. Mason, S.A. Barnett, J. Vac. Sci. Tech. A: Vacuum, Surfaces, and Films **9**, 1991 (1991)
23. P.S. Manning, J.D. Sirman, R.A. De Souza, J.A. Kilner, Solid State Ionics **100**, 1 (1997)
24. T. Petrovsky, H.U. Anderson, V. Petrovsky, Mater. Res. Soc. Symp. Proc. **756**, EE4.7.1 (2003)
25. W. Jung, H.L. Tuller, J. Electrochem. Soc. **155**, B1194 (2008)
26. F.S. Baumann, J. Fleig, G. Cristiani, B. Stuhlhofer, H.-U. Habermeier, J. Maier, J. Electrochem. Soc. **154**, B931 (2007)
27. F.S. Baumann, J. Fleig, H.-U. Habermeier, J. Maier, Solid State Ionics **177**, 1071 (2006)
28. W.C. Chueh, S.M. Haile, Phys. Chem. Chem. Phys: PCCP **11**, 8144 (2009)
29. N. Imanishi, T. Matsumura, Y. Sumiya, K. Yoshimura, A. Hirano, Y. Takeda, D. Mori, R. Kanno, Solid State Ionics **174**, 245 (2004)
30. J. Maier, *Physical Chemistry of Ionic Materials* (Wiley, Chichester, 2004)
31. B.C.H. Steele, Solid State Ionics **75**, 157 (1995)
32. R.A. De Souza, J.A. Kilner, Solid State Ionics **126**, 153 (1999)
33. W. Jung, *A New Model Describing Cathode Kinetics in Solid Oxide Fuel Cell: Model Thin Film $SrTi_{1-x}Fe_xO_{3-\delta}$ Mixed Conducting Oxides – a case study, in Department of Materials Science and Engineering* (Massachusetts Institute of Technology, Cambridge, 2010)